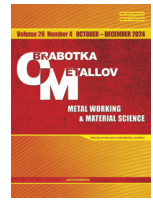**Obrabotka metallov -**

Metal Working and Material Science

Journal homepage: http://journals.nstu.ru/obrabotka_metallov

Geometry distortion, edge oxidation, structural changes and cut surface morphology of 100mm thick sheet product made of aluminum, copper and titanium alloys during reverse polarity plasma cutting

Artem Grinenko [1, a], Andrey Chumaevsky [2, b, *], Evgeny Sidorov [2, c], Veronika Utyaganova [2, d], Alihan Amirov [2, e], Evgeniy Kolubaev [2, f]

[1] ITS-Siberia LLC, Krasnoyarsk, 16a Severnoe shosse, 660118, Russian Federation
[2] Institute of Strength Physics and Materials Sciences SB RAS, 2/4, pr. Akademicheskii, Tomsk, 634055, Russian Federation

[a] https://orcid.org/0009-0002-9511-1303, giga2011@yandex.ru; [b] https://orcid.org/0000-0002-1983-4385, tch7av@gmail.com;
[c] https://orcid.org/0009-0009-2665-7514, eas@ispms.ru; [d] https://orcid.org/0000-0002-2303-8015, veronika_ru@ispms.ru;
[e] https://orcid.org/0000-0002-5143-8235, amir@ispms.tsc.ru; [f] https://orcid.org/0000-0001-7288-3656, eak@ispms.tsc.ru

---

ARTICLE INFO

ABSTRACT

The introduction describes the feasibility of using reverse polarity plasma cutting to produce large-sized non-ferrous metal blanks up to 100 mm thick. Data on the use of plasma cutting with direct and reverse polarity currents for thick sheet metal and the main technological problems associated with its implementation are presented. **The purpose of the work** is to study the organization of the structure and properties of the near-surface zone, changes in the chemical and phase composition when cutting aluminum, copper and titanium alloys. The research methods are optical and scanning electron microscopy, microhardness measurement, X-ray diffraction and energy-dispersive analysis. Plasma cutting was carried out using air as a plasma-forming and shielding gas, simultaneously with water injection into the discharge chamber and the formation of a "water fog" around the plasma column. **Results and discussion.** It is shown that both the arc stability and the shape of the plasma column are of great importance in reverse polarity plasma cutting of rolled sheets. The distortion of the cutting geometry during normal operation is greatest in the central part, and with insufficient heat input it shifts to the lower part and increases significantly. The operation of the plasma torch in air does not lead to significant changes in the composition of the cutting surface of aluminum and copper alloys. A decrease in the magnesium content near the edge is typical for the aluminum alloy in the surface layers. Cutting of the titanium alloy is accompanied by intense oxidation of the surface, especially in areas of difficult metal displacement from the cutting cavity. The formation of titanium oxides, mainly rutile Ti_2O, sharply increases the microhardness values in the surface layers, which negatively affects the machinability of the cutting edge and requires shot blasting to remove the oxide layer. **The conclusion** describes the main patterns of implementing reverse polarity plasma cutting of sheet metal from aluminum, copper and titanium alloys with a thickness of 100 mm.

---

* Corresponding author
Chumaevsky Andrey V., D.Sc. (Engineering), Leading researcher,
Institute of Strength Physics and Materials Sciences SB RAS,
2/4, pr. Akademicheskii,
634055, Tomsk, Russian Federation
Tel.: +7 (382) 228-68-63, **e–mail:** tch7av@ispms.ru

Introduction

Currently, one of the pressing challenges in domestic industry is the need for high-efficiency production of non-ferrous metal and alloy blanks for the fabrication of large-scale components and structures. Flame cutting and waterjet cutting methods are capable of cutting thick sheet metal but suffer from low performance [1-3]. Laser cutting offers high performance but is not suitable for producing thick-section blanks [4, 5]. Conventional mechanical cutting methods do not have the necessary flexibility for manufacturing complex-shaped parts.

Plasma cutting combines high performance with the ability to process thick sheet metal [6-8]. This method is well-suited for both steels and ferrous metals [9, 10], as well as copper, aluminum, and titanium alloys [11-16]. Plasma cutting can produce blanks from thick sheet metal, including materials with thicknesses of 100 mm or more. However, cutting such thick blanks using plasma torches operating on direct polarity current presents significant challenges and leads to considerable wear of the working elements [17, 18]. Moreover, most of the available plasma torches of this type are produced by foreign manufacturers and are not domestically manufactured. Therefore, there is a need to develop alternative plasma cutting equipment of domestic origin. For this purpose, a joint project between the Institute of Strength Physics and Materials Sciences (ISPMS SB RAS) and LLC ITS-Siberia is currently focused on developing equipment for reverse polarity plasma cutting of thick sheet non-ferrous metals and alloys [13-16, 18, 19].

Reverse polarity plasma cutting offers several advantages over direct polarity. First of all, the consumption of nozzles and electrodes included in the plasma torches is reduced [17, 18]. The second, but no less important factor, is the increase in the thickness of sheet metal that can be cut [15]. Reverse polarity plasma cutting also delivers higher performance at the same power level compared to direct polarity [18, 20-23]. Additionally, it improves the quality of the cut surface and reduces the extent of structural changes caused by thermal effects [18]. However, reverse polarity plasma cutting is more complex in terms of optimizing cutting parameters [13-16] and involves specific challenges related to the degradation and wear of plasma torch components [18].

Despite the fairly long history of using plasma cutting, there is almost no information in the modern literature regarding the effects of the cutting process on the structure and surface quality of sheet metal with a thickness of 100 mm or more when using reverse polarity plasma torches.

The *aim of this study* is to investigate the structural organization, edge distortion, and changes in chemical and phase composition during reverse polarity plasma cutting of aluminum, copper, and titanium alloys.

Materials and methods

Experimental studies were carried out at the production site of LLC ITS-Siberia and on experimental equipment at the Institute of Strength Physics and Materials Sciences (ISPMS SB RAS). The cutting process was performed using a reverse polarity plasma torch developed as part of a joint scientific and technical project. The materials used were 100 mm thick plates of *Al-6Mg* aluminum alloy, *Cu-9Al-2Mn* bronze, and *Ti-5Al-5Mo-5V* titanium alloy in its as-received condition. The schematic of the plasma torch operation and the plasma cutting process is shown in Fig. 1, *a*.

The cutting of 100 mm thick plates (**1**) was performed using a plasma jet (**2**) formed in a protective gas environment (**3**), initiated by the pilot arc (**4**) at the start of the process and maintained by the main arc (**5**) during the cutting operation. The supply of the protective and plasma-forming gas (**6**) to the cutting zone was maintained at a fixed pressure in the system. The nozzle (**7**) was secured with a nut (**8**). Inside the nozzle, a dense vortex stream of gas and plasma (**9**) was formed, driven by the swirl generator (**10**) and arc combustion. Additionally, in the developed plasma torch design, water injection (**11**) into the discharge chamber was implemented through an opening in the working electrode (**14**). This setup was necessary to improve cut quality and reduce nozzle and electrode wear [16, 18, 19]. To prevent overheating of the nozzle and electrode, a constant flow of water (**12**) was maintained through channels in the torch body (**13**). Due
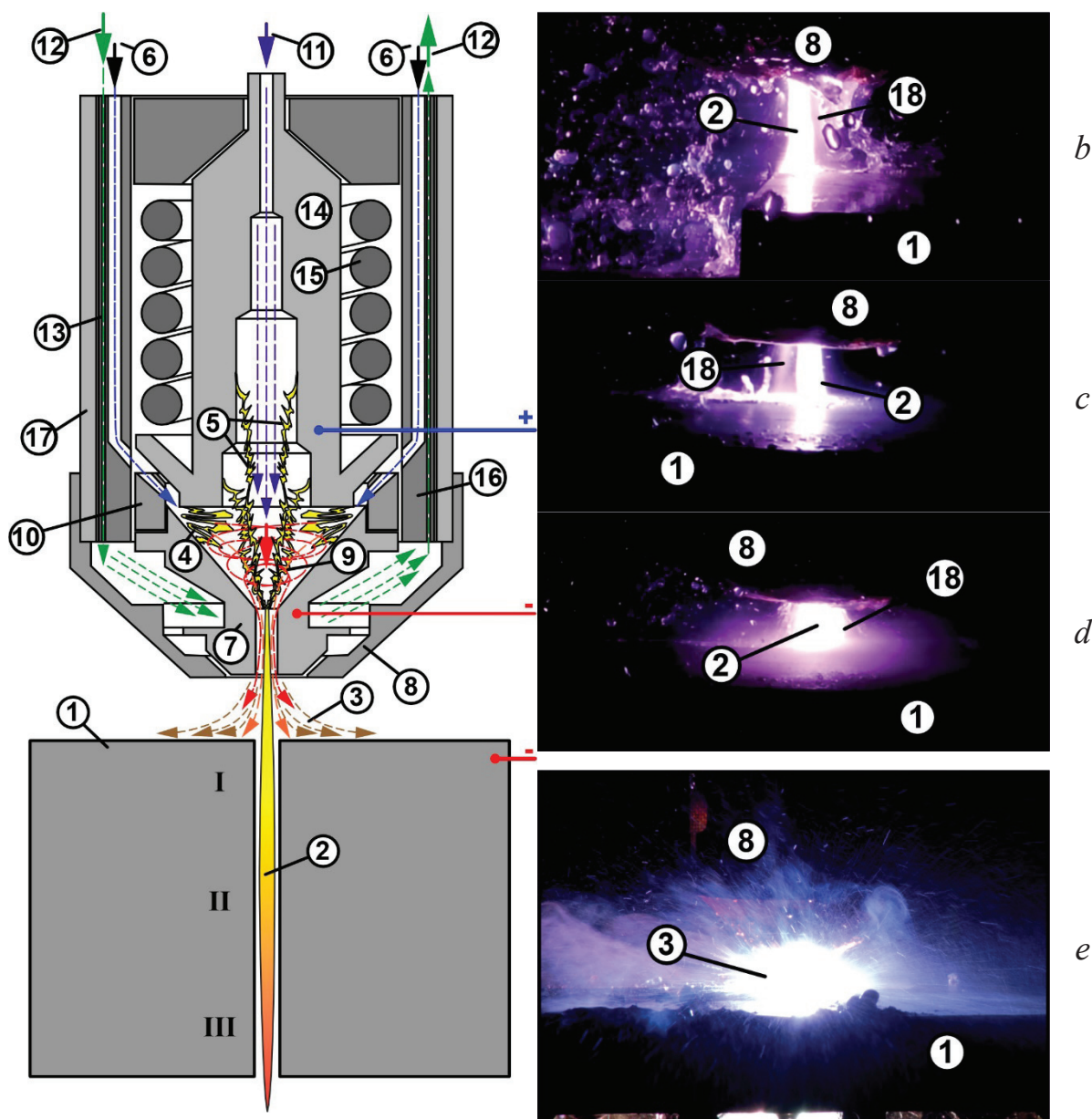
Fig. 1. Scheme of the reverse polarity plasma torch operation (*a*); the appearance of the plasma jet at start (*b*) and in the operating mode (*c*); an increase in the density of the "water mist" around the plasma jet (*d*); and the appearance of the cutting zone (*d*):

1 – plate; *2* – plasma jet; *3* – gas flow; *4* – starting arc; *5* – working arc; *6* – flow of plasma-forming and protective gas; *7* – nozzle; *8* – external nut; *9* – vortex flows of gas and plasma; *10* – swirler; *11* – water supply to the hollow electrode; *12* – supply of cooling water to the plasma torch body; *13* – water cooling channels; *14* – electrode; *15* – solenoid; *16* – inner casing made of *PTFE*; *17* – outer steel casing; *18* – "water mist"

to the design features of the plasma torch, the water flow (**13**) first passed through the nozzle and electrode, and then partially exited the torch body and partially entered the discharge chamber. Current was supplied to the electrode via a copper solenoid (**15**), which also generated a magnetic field to focus the plasma jet and electric arc. The inner torch body (**16**), with water and air supply channels, was made of fluoroplastic, while the outer body (**17**) was made of steel. The working electrode (**14**) and nozzle (**7**) were made of *M1*-grade copper (*Cu-ETP*).

At the start of the process, the distance between the plasma torch and the plate was increased (Fig. 1, *b*), and after arc stabilization, it was reduced (Fig. 1, *c*). During cutting, the "water mist" around the plasma jet varied significantly due to pressure pulsations in the discharge chamber (Fig. 1, *c*, *d*). A large amount of

metal combustion products accumulated around the cutting zone, which were displaced by the protective gas flow (Fig. 1, *e*). The arc current during cutting ranged from 350 to 370 A, with a voltage ranged from 370 to 400 V. The height of the plasma torch above the plate surface during cutting was from 16 to 25 mm. Gas pressure ranged from 2.0 to 4.0 bar, and water pressure in the system before entering the plasma torch cooling circuit was 6 bar. The gap between the nozzle and electrode was between 0.5 and 2.0 mm. The cutting speed varied from 250 to 3,000 mm/min. Air was used as both the plasma-forming and protective gas.

After obtaining the experimental samples, metallographic sections for structural analysis were cut from it using electrical discharge machining (*DK7750 machine*). Structural and morphological studies of the cut surface were conducted using an optical microscope *Altami MET 1C*, *Olympus LEXT 4100* laser scanning microscope, and *Zeiss LEO EVO 50* scanning electron microscope equipped with a system for micro-X-ray spectral analysis. The distortion of the cut geometry was determined by the maximum deviation of the cut surface from perpendicularity, using macrostructural images obtained through optical microscopy.

The most pronounced edge distortion for the aluminum and copper alloys occurred in the central region (**II** in Fig. 2, *b*, *c*), whereas for the titanium alloy, the greatest distortion was observed at the lower edge (**III** in Fig. 2, *d*). The roughest surface texture for all alloy samples was seen at the bottom of the plate (**III**), while the most uniform cut surface was in the upper region (**I**). In the subsurface structure of all three alloy types, there were regions of molten metal, a heat-affected zone (*HAZ*), and the base metal with an unchanged structure. The structure of the *Cu-9Al-2Mn* bronze was the least affected by thermal exposure, while the *Ti-5Al-5Mo-5V* alloy exhibited the largest *HAZ*, and the *Al-6Mg* alloy had the thickest molten metal zone. As will be discussed later, these differences are due to the thermal conditions, alloy composition, melting temperatures, and thermal conductivity.

Results and discussion

During plasma cutting of 100 mm thick plates, a specific structure formed near the cut surface, along with a characteristic macroscopic relief typical of plasma cutting (Fig. 2). The cut surfaces of the aluminum alloy and bronze exhibited numerous flow marks from the metal along the cut edge during the cutting process (Fig. 2, *a*, *c*). The cut surface of the titanium alloy, however, showed fewer signs of metal flow and was characterized by the presence of microcracks (Fig. 2, *e*).

The most pronounced edge distortion for the aluminum and copper alloys occurred in the central region (**II** in Fig. 2, *b*, *d*), whereas for the titanium alloy, the greatest distortion was observed at the lower edge (**III** in Fig. 2, *e*). The roughest surface texture for all alloy samples was seen at the bottom of the plate (**III**), while the most uniform cut surface was in the upper region (**I**). In the subsurface structure of all three alloy types, there were regions of molten metal, a heat-affected zone (*HAZ*), and the base metal with an unchanged structure. The structure of the *Cu-9Al-2Mn* bronze was the least affected by thermal exposure, while the *Ti-5Al-5Mo-5V* alloy exhibited the largest *HAZ*, and the *Al-6Mg* alloy had the thickest molten metal zone. As will be discussed later, these differences are due to the thermal conditions, alloy composition, melting temperatures, and thermal conductivity.

The surface of the *Al-6 Mg* aluminum alloy after cutting exhibits different structures in the upper, central, and lower parts of the cut (Fig. 3, *a–c*). The upper part is more uniform, while the lower part contains a higher number of pores and oxidation marks. Microstructural analysis revealed the formation of microcracks (**1** in Fig. 3, *d*) and small spherical pores (**2** in Fig. 3, *d*). Energy-dispersive spectroscopy (*EDS*) indicated a significant amount of oxygen in the surface layers. The surface layer structure (Fig. 4, *a–e*) shows distinct regions: the fusion zone (*FZ*), the heat-affected zone (*HAZ*), and the base metal (*BM*). The depth of the heat-affected zone (*HAZ*) and base metal (*BM*) does not exceed 1 mm in the central part. The fusion zone (*FZ*) contains a large number of coarse secondary phase particles (**1** in Fig. 4, *d*), pores (**2** in Fig. 4, *f*, g), and discontinuities (**3** in Fig. 4, *g*). According to energy-dispersive spectroscopy (*EDS*) analysis, the fusion zone contains only a small amount of oxygen, but there is a significant change in magnesium content, as shown in Fig. 5, *b*. The depletion of magnesium in *Al-6 Mg* -type alloys is expected

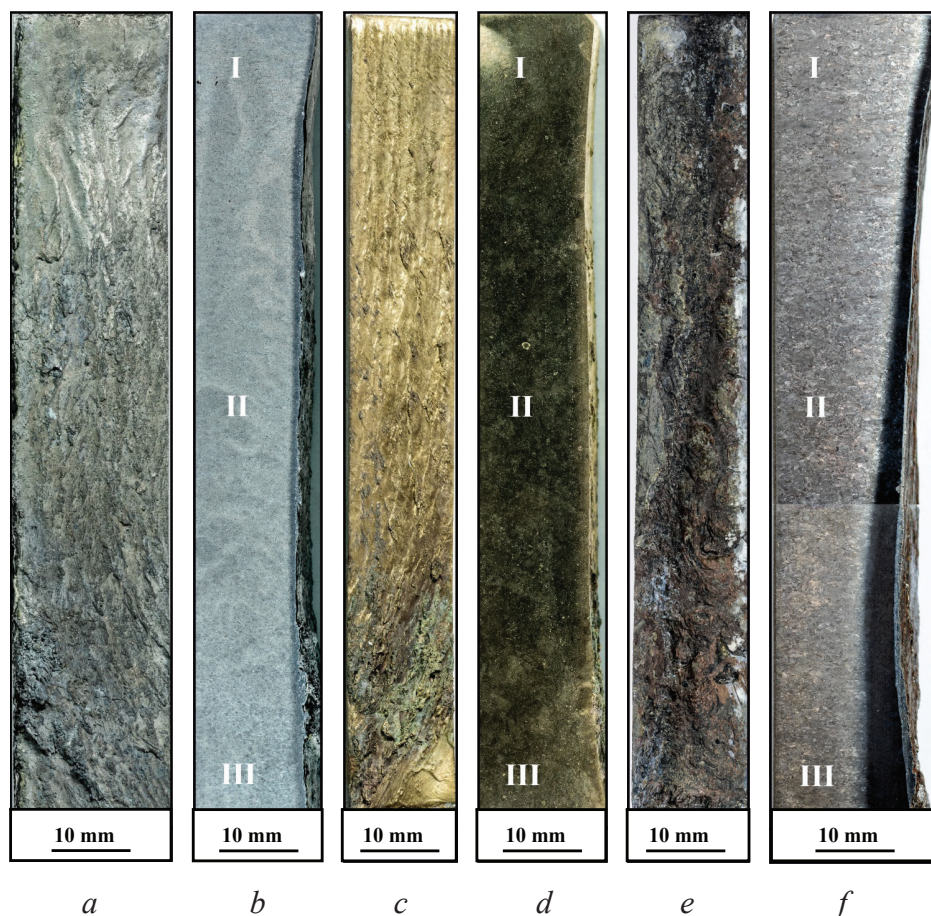*Fig. 2.* The cut surface (*a, c, e*) and the macrostructure in the cross section (*b, d, f*) of specimens of aluminum alloy *Al-6 Mg* (*a, b*), bronze *Cu-9 Al-2 Mn* (*c, d*) and titanium alloy *Ti-5 Al-5 Mo-5 V* (*e, f*) after reverse polarity plasma cutting
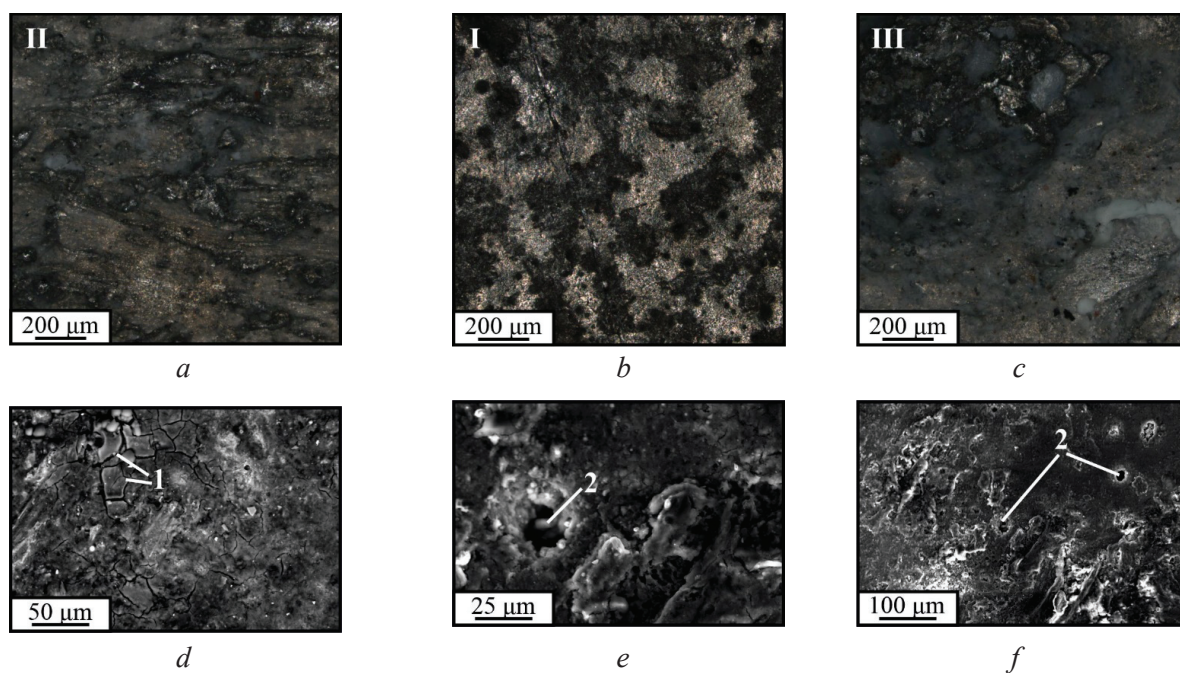

Fig. 3. Images of the cut surface of aluminum alloy *Al-6 Mg* obtained by laser scanning (*a–c*) and scanning electron (*d–e*) microscopy
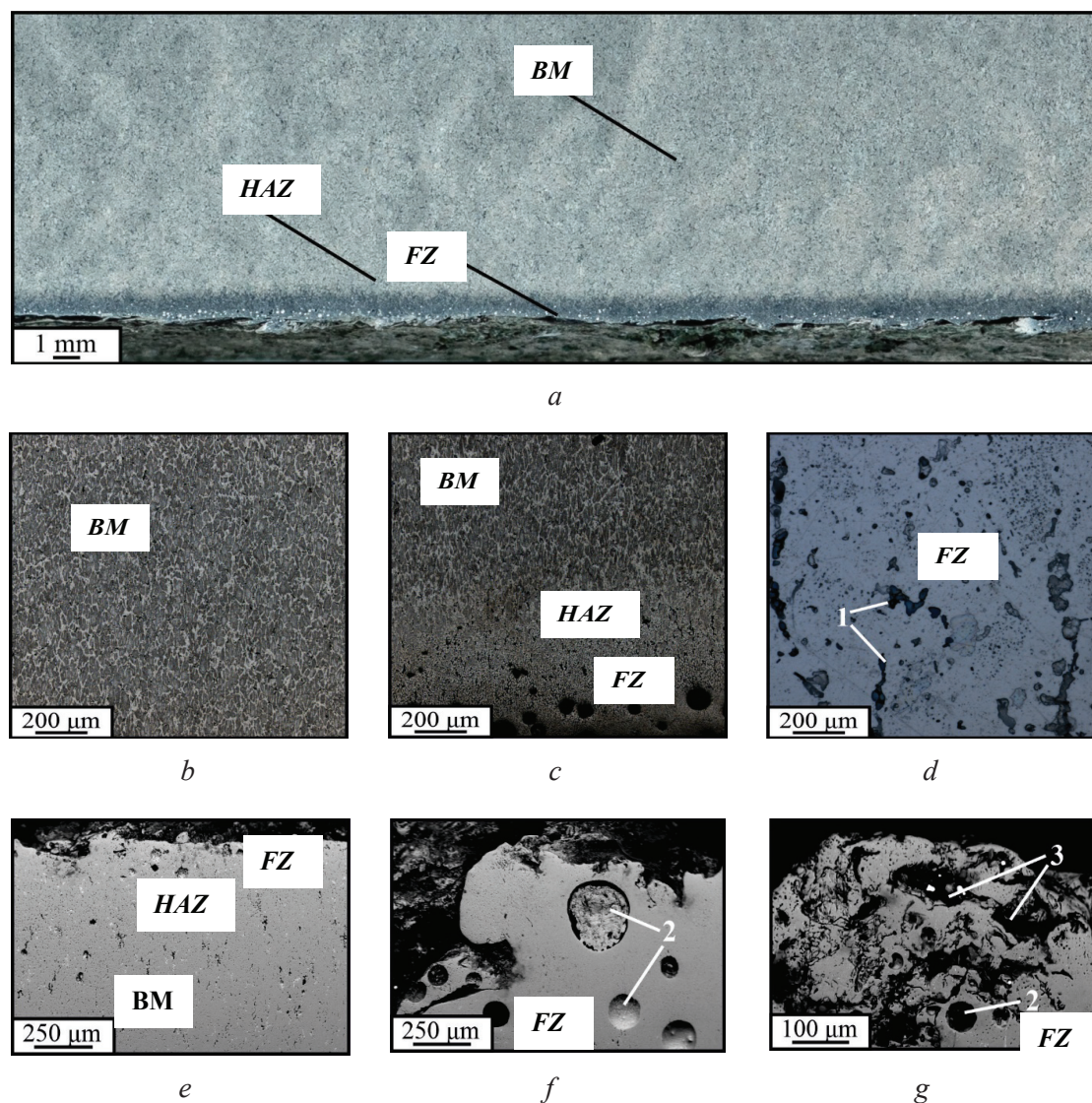
Fig. 4. Macrostructure (*a*), images of the microstructure obtained by optical (*b*–*d*) and scanning electron (*e*–*g*) microscopy of a specimen of aluminum alloy *Al-6 Mg*

and is also observed during welding by various methods. X-ray diffraction (*XRD*) analysis indicated that no phase composition changes occur in the surface layers, and the structure remains *Al(Mg)* (Fig. 5, *c*, *d*).

Due to the removal of work hardening and the depletion of magnesium in the surface layers of the aluminum alloy, there is a significant reduction in microhardness, especially in the lower part of the cut (Fig. 5, *a*). In the upper part of the cut, microhardness decreases from 1.21 GPa in the base metal to 1.01 GPa in the subsurface zone, whereas in the lower part, it reaches approximately 0.94 GPa near the surface. In both the upper and central regions of the cut, at a depth of 1.0 mm, the microhardness returns to values typical of the base metal, but in the lower part, it remains at 1.05 GPa. This indicates a significantly greater thermal impact on the material in the lower section of the cut, due to the displacement of molten metal through this area and the difficulty in removing it with the protective gas stream. Overall, considering the dimensional tolerances for producing blanks from plates of this thickness, both the cut distortion and the structural changes can be considered acceptable.

The surface of the *Cu-9 Al-2 Mn* bronze after cutting also exhibits significant variations in relief across the upper, lower, and central parts of the cut zone (Fig. 6, *a-c*). Distinct features are identified, formed by the rapid solidification of metal flowing down the edge during cutting (**1** in Fig. 6, *d*). Additionally, scanning electron microscopy (*SEM*) and X-ray diffraction (*XRD*) analysis reveal fragments of oxides (**2** in Fig. 6, *e*) and formations resembling pores or "craters" (**3** in Fig. 6, *f*). The oxidation of the surface is patchy, and a continuous oxidized layer does not form.
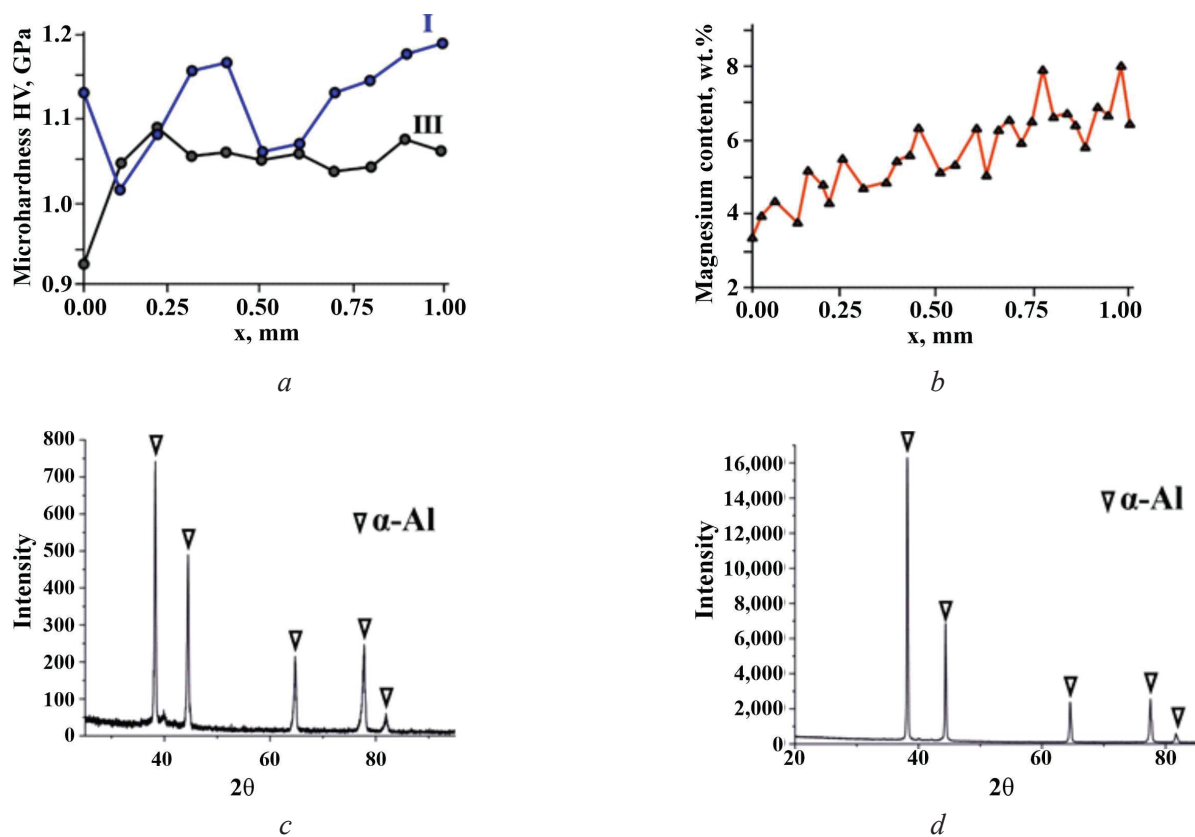
Fig. 5. Microhardness (*a*), change in magnesium content (*b*) in the surface layers of aluminum alloy *Al-6 Mg* and the results of X-ray analysis of the base metal (*c*) and the cut surface (*d*)
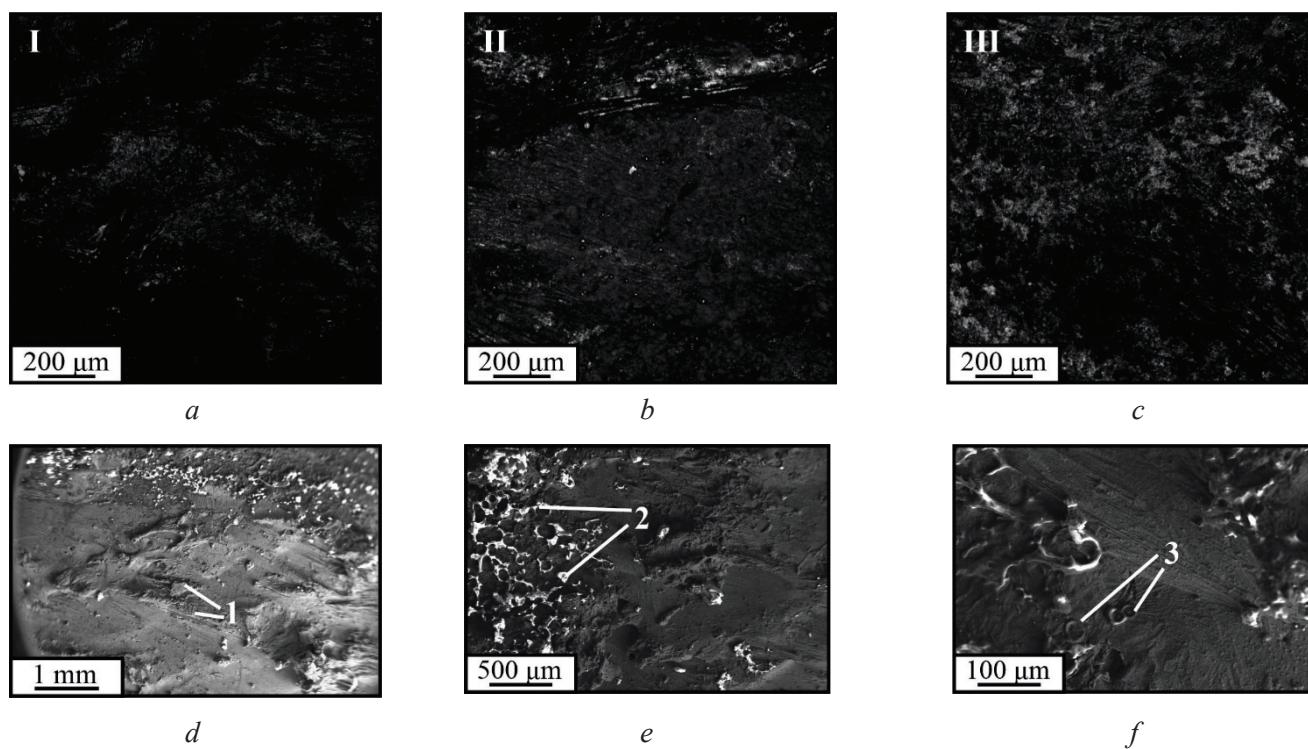

Fig. 6. Images of the cut surface bronze *Cu-9 Al-2 Mn* obtained by laser scanning (*a–c*) and scanning electron (*d–f*) microscopy

The structure of the surface layer also includes a melting zone, a heat-affected zone, and the base metal (Fig. 7, *a-d*). Within the materials of these zones, there are pores (**1** in Fig. 7, *e*) and discontinuities (**2** in Fig. 7, *g*). However, the molten metal zone is significantly smaller, with a thickness not exceeding 100-200 μm in the central part, while the heat-affected zone is only weakly defined (Fig. 7, *a-d*, Fig. 8, *a*). The microhardness values in the surface layers show minimal variation, which can be attributed to the high thermal conductivity of the material and rapid cooling. Consequently, energy dispersive spectroscopy (*EDS*) analysis indicates that no qualitative changes in the phase composition occur within the material (Fig. 8, *b, c*). The primary phase consists of a solid solution of *Cu(Al)* and the β'-phase (needle-like Cu_3Al present between the grains of the solid solution). In the melting and heat-affected zones, only changes in the volume fraction and concentration of these phases can be identified (Fig. 7, *c, f*). Additionally, secondary phases appear as particles of Cu_3Al throughout the material. The high thermal conductivity of the material leads to lesser structural changes in the near-surface zone compared to the aluminum alloy, while also resulting in a larger proportion of material not displaced from the cutting zone in the lower part of the cut, as illustrated in Fig. 2, *c*. Overall, based on the analysis of geometric distortion and structural changes in the material for plates of this size, the quality of the cut can be considered acceptable.

The morphology of the cut surface of the *Ti-5Al-5Mo-5V* titanium alloy in the upper, lower, and central regions is fairly consistent (Fig. 9, *a-c*). Unlike copper and aluminum alloys, the surface topography in this case exhibits only minimal traces of the material following the contour of the tool. However, there are
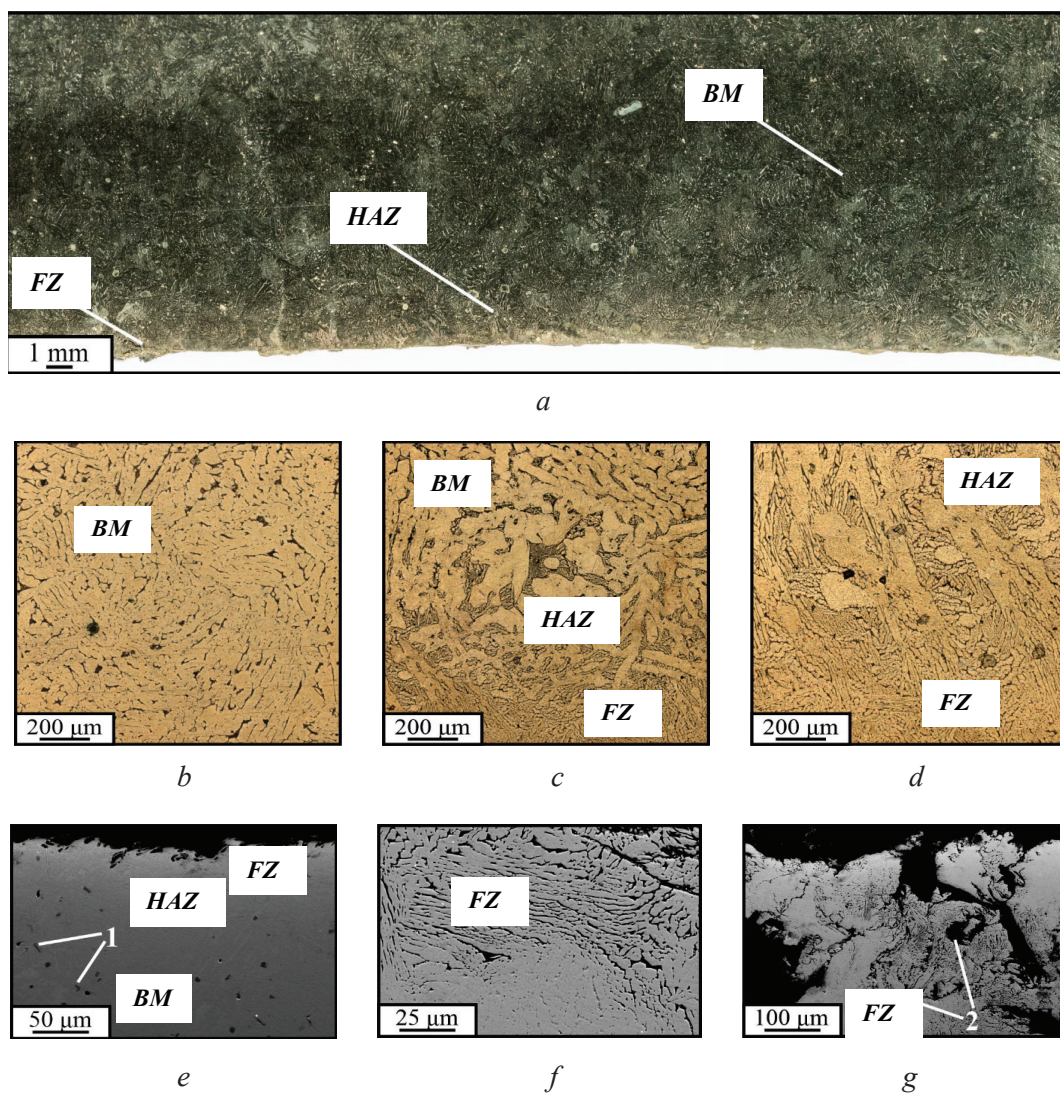

Fig. 7. Macrostructure (*a*), images of the microstructure obtained by optical (*b–d*) and scanning electron (*e–g*) microscopy of a specimen of bronze *Cu-9 Al-2 Mn*
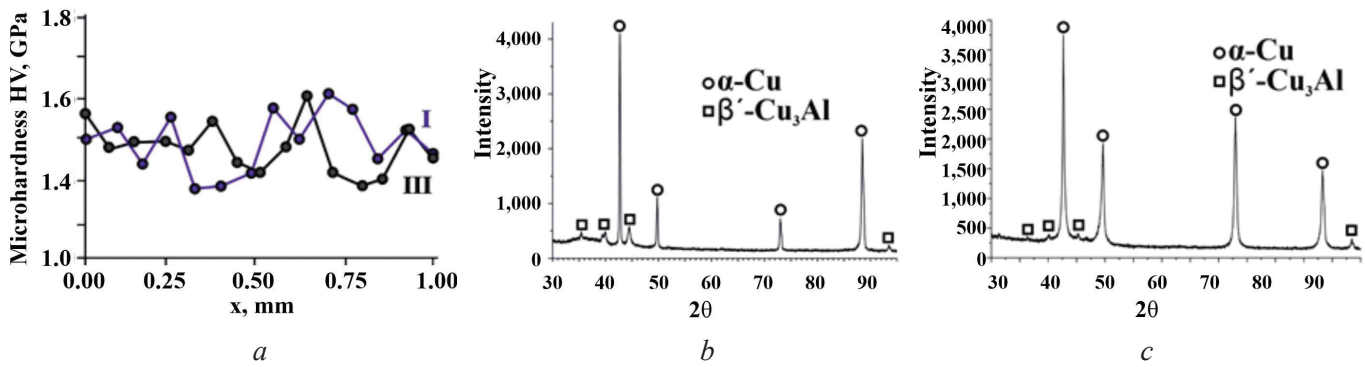
Fig. 8. Change in microhardness in the surface layers of bronze *Cu-9 Al-2 Mn* (*a*) and the results of X-ray analysis of the base metal (*b*) and the cut surface (*c*)
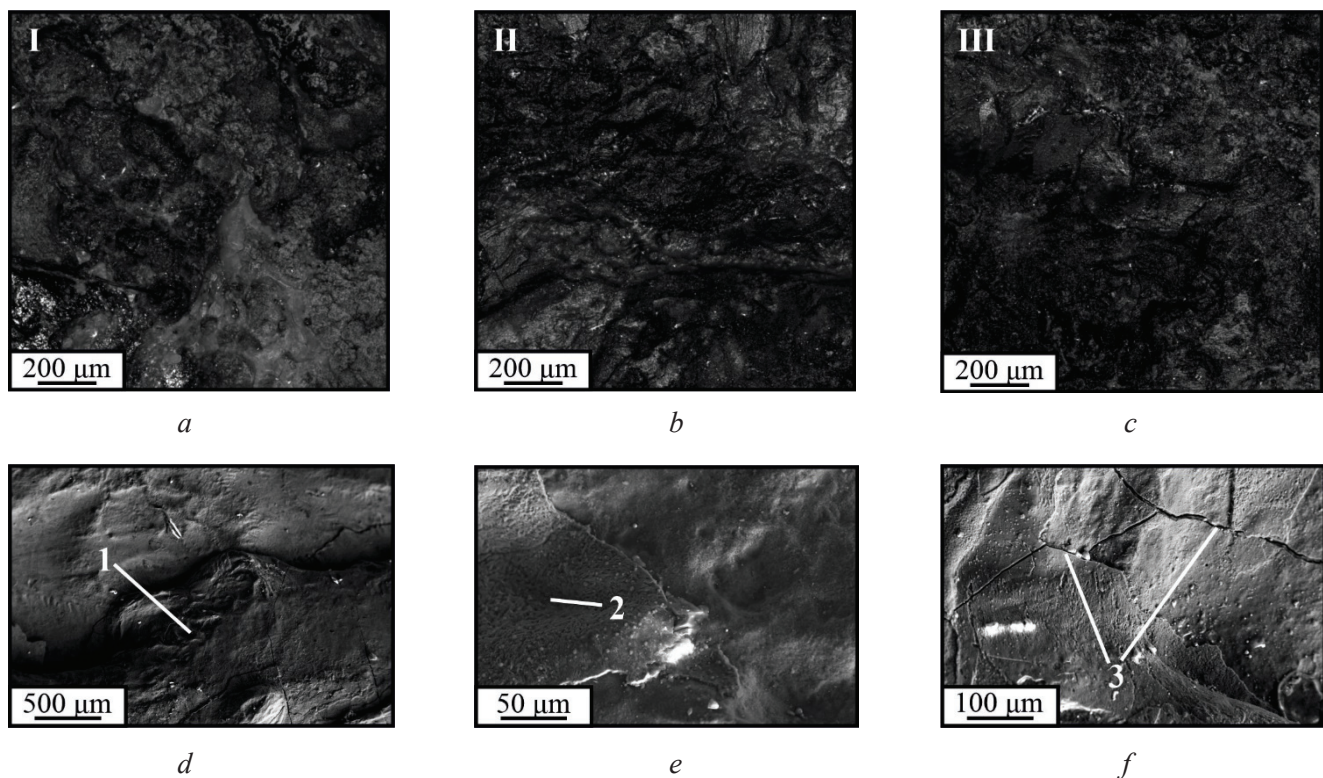

Fig. 9. Images of the cut surface of titanium alloy *Ti-5 Al-5 Mo-5 V* obtained by laser scanning (*a–c*) and scanning electron (d–*f*) microscopy

similarly shaped protrusions in the central part of the cut (marked as **1** in Fig. 9, *d*). The primary reason for the distinctive morphology of the titanium alloy cut surface is the oxidation of the surfaces, which results in the formation of a continuous oxide layer, as confirmed by *SEM* and *EDS* analysis (Fig. 9, *e*, *f*). According to *EDS* and X-ray diffraction (*XRD*) analysis, the main oxide phase is Ti_2O (Fig. 11, *d*). The surface layer may also contain dendritic structures that formed during the crystallization of the oxide (marked as **2** in Fig. 9, *e*), as well as microcracks (marked as **3** in Fig. 9, *f*), the formation of which occurred during the cooling of the material after cutting. Structural and chemical analysis of the material shows that the melt zone is stable and that oxidation extends across nearly the entire surface (Fig. 10, *a*; Fig. 11, *b*), penetrating up to 0.5 mm into the lower part of the cut.

The material in the cross-section is also characterized by the presence of a melt zone, a heat-affected zone (*HAZ*), and the base metal (Fig. 10, *a-d*). During the melting of titanium and its oxides, dendritic structures form. Both the base metal and the heat-affected zone exhibit alpha and beta-phase lamellae, as
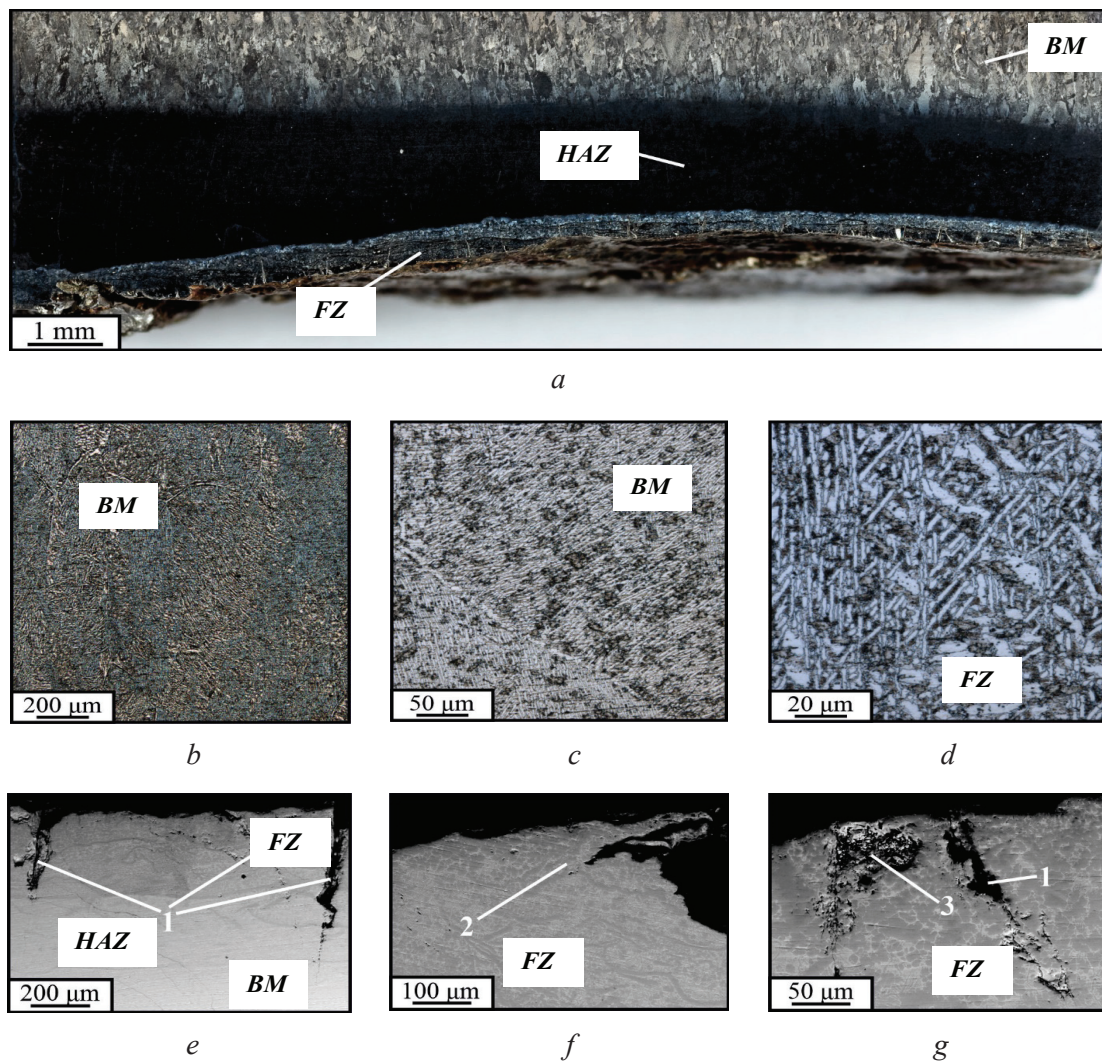
Fig. 10. Macrostructure (*a*), images of the microstructure obtained by optical (*b–г*)
and scanning electron (*e–g*) microscopy of a specimen of titanium alloy
Ti-5 Al-5 Mo-5 V

confirmed by optical microscopy (Fig. 10, *b*, *c*) and *XRD* analysis (Fig. 11, *c*, *d*). The melt zone contains relatively large cracks throughout its length (marked as **1** in Fig. 10, *e*).

Near the surface within the fusion zone, the presence of protrusions (marked as **2** in Fig. 10, *f*) and discontinuities (marked as **3** in Fig. 10, *g*) can be identified. Due to oxidation in the subsurface layers, there is a noticeable increase in microhardness (Fig. 11, *a*). The most significant increase in microhardness, reaching up to 8 GPa, occurs in the lower part of the cut zone, with the depth of this zone exceeding 1 mm in this case. In contrast, in the upper part of the cut, both the thermal impact on the material and the degree of edge oxidation are significantly lower, with the depth of these affected zones not exceeding 0.3 mm.

The oxidation of the titanium alloy in the surface layers is more pronounced compared to that of aluminum alloys, which is attributed to the higher reactivity of titanium and its melting temperature. In the lower part of the cut zone, at the set power of the plasma-generating arc, the complete penetration of the plasma jet through the plate was hindered, resulting in prolonged thermal exposure to the material.

It can be determined that in this case, the cut was formed at the limit of the process capability, on the verge of full penetration of the plate and the occurrence of a defect in the form of incomplete cutting. This resulted in more significant oxidation of the edge in the lower part and a deterioration in the overall cut quality. For machining titanium alloy workpieces, this is generally unacceptable, and post-cutting shot blasting is required to remove the scale after plasma cutting. The use of nitrogen as a shielding and plasma-generating gas is also possible, but for plates of this thickness, slow cooling of the edge is characteristic,
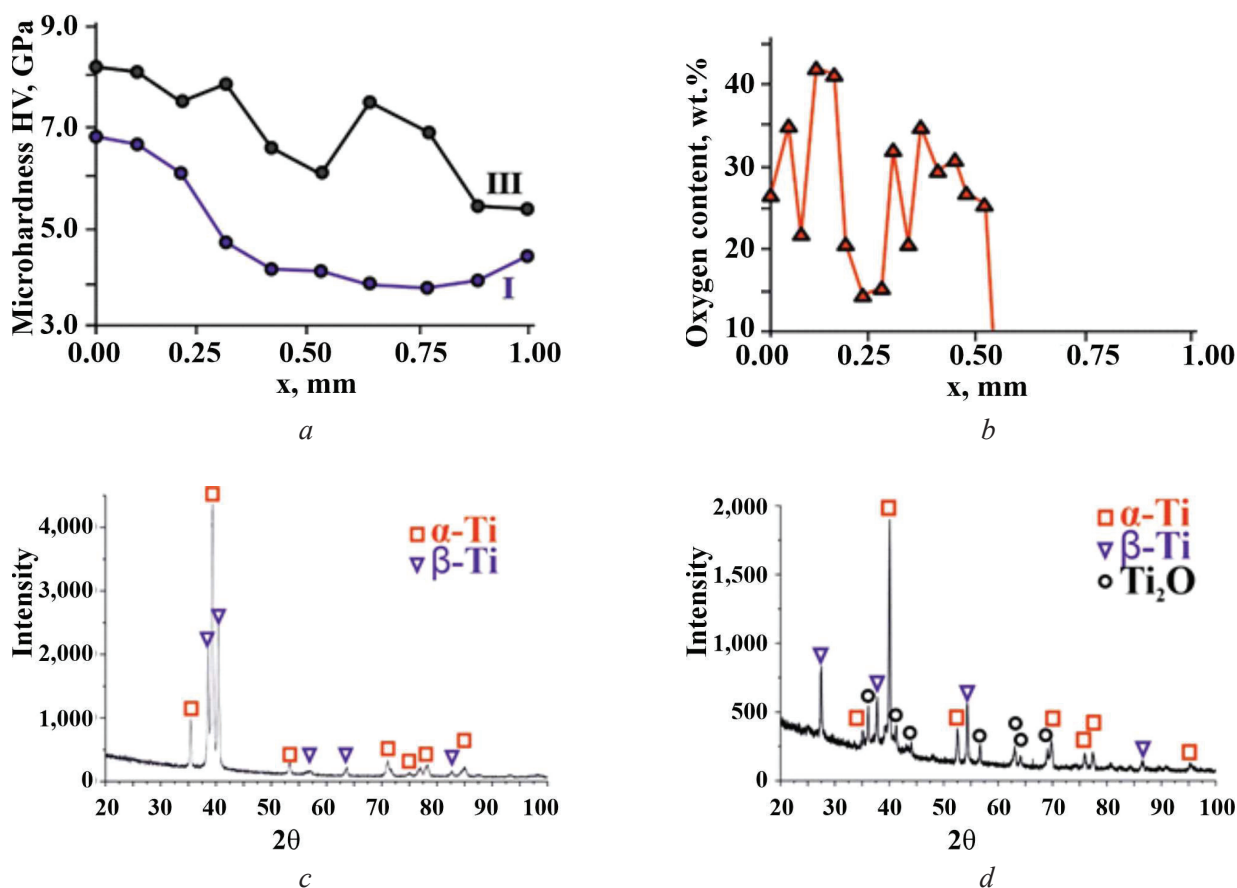
Fig. 11. Microhardness (*a*), change in oxygen content (*b*) in the surface layers of titanium alloy
Ti-5Al-5Mo-5V and the results of X-ray analysis of the base metal (*c*) and the cut surface (*d*)

particularly for titanium alloys with relatively low thermal conductivity. This makes it difficult to avoid edge oxidation due to insufficient metal removal from the kerf and excessive melting of the surface. However, increasing the power of the plasma arc source and cutting at a slightly higher current (around 400 A) could allow for acceptable quality cuts on titanium alloy plates up to 100 mm thick, even when using air as the plasma-generating gas.

Conclusion

The conducted studies demonstrate that it is possible to obtain 100 mm thick blanks from sheet rolled aluminum, copper and titanium alloys using the reverse polarity plasma cutting. The best surface quality of the cut is observed in the *Al-6Mg* aluminum alloy and *Cu-9 Al-2 Mn* bronze. These alloys exhibit only minor changes in mechanical properties and surface layer structure, as well as minimal geometric distortions in the cut. The zone with reduced magnesium content in the aluminum alloy does not exceed 0.5 mm from the cut surface, while in bronze, there is virtually no change in chemical composition. Both alloys show the presence of oxygen only on the cut surface without the formation of an oxide layer. In contrast, the quality of the *Ti-5Al-5Mo-5V* titanium alloy cut is significantly lower. Due to the higher melting temperature, achieving full penetration of the plate is more challenging, and significant edge distortion can be observed in the lower part of the plate. A substantial oxide layer forms on the surface, within which microcracks develop during cooling. This necessitates the requirement for shot blasting post-processing of the titanium alloy after cutting when air is used as the plasma-forming gas, or alternatively, replacing air with nitrogen. It is also noteworthy that in the upper part of the cut zone, where metal displacement from the kerf is more efficient, the oxide layer is relatively thin. Cutting in air with additional water injection for the titanium alloy can also be employed but would likely require higher arc power and gas pressure.

References

1. Levichev N., Tomás García A., Dewil R., Duflou J.R. A virtual sensing approach for quality and productivity optimization in laser flame cutting. *The International Journal of Advanced Manufacturing Technology*, 2022, vol. 121, pp. 6799–6810. DOI: 10.1007/s00170-022-09750-8.

2. Barsukov G.V., Selemenev M.F., Zhuravleva T.A., Kravchenko I.N., Selemeneva E.M., Barmina O.V. Influence of the parameters of chemical thermal treatment of copper slag particles on the quality of hydroabrasive cutting. *Journal of Machinery Manufacture and Reliability*, 2023, vol. 52, pp. 679–686. DOI: 10.1134/S1052618823070075.

3. Barsukov G., Zhuravleva T., Kozhus O. Quality of hydroabrasive waterjet cutting machinability. *Procedia Engineering*, 2017, vol. 206, pp. 1034–1038. DOI: 10.1016/j.proeng.2017.10.590.

4. Wei J., He W., Lin C., Zhang J., Chen J., Xiao J., Xu J. Optimizing process parameters of in-situ laser assisted cutting of glass-ceramic by applying hybrid machine learning models. *Advanced Engineering Informatics*, 2024, vol. 62, p. 102590. DOI: 10.1016/j.aei.2024.102590.

5. Shulyat'ev V.B., Gulov M.A., Karpov E.V., Malikov A.G., Boiko K.R. Laser cutting of aluminum alloys using pulsed radiation from a CO_2 laser under conditions of an optical discharge in an argon jet. *Bulletin of the Lebedev Physics Institute*, 2023, vol. 50, pp. S1075–S1078. DOI: 10.3103/S1068335623220116.

6. He G.-J., Gu L., Zhu Y.-M., Chen J.-P., Zhao W.-S., Rajurkar K.P. Electrical arc contour cutting based on a compound arc breaking mechanism. *Advances in Manufacturing*, 2022, vol. 10 (4), pp. 583–595. DOI: 10.1007/s40436-022-00406-0.

7. Sharma D.N., Kumar J.R. Optimization of dross formation rate in plasma arc cutting process by response surface method. *Materials Today: Proceedings*, 2020, vol. 32, pp. 354–357. DOI: 10.1016/j.matpr.2020.01.605.

8. Ilii S.M., Coteata M. Plasma arc cutting cost. *International Journal of Material Forming*, 2009, vol. 2, pp. 689–692. DOI: 10.1007/s12289-009-0588-4.

9. Cinar Z., Asmael M., Zeeshan Q. Developments in plasma arc cutting (PAC) of steel alloys: a review. *Jurnal Kejuruteraan*, 2018, vol. 30, pp. 7–16. DOI: 10.17576/jkukm-2018-30(1)-01.

10. Barcelos M.B., Almeida D.T. de, Tusset F., Scheuer C.J. Performance analysis of conventional and high-feed turning tools in machining the thermally affected zone after plasma arc cutting of low carbon manganese-alloyed steel. *Journal of Manufacturing Processes*, 2024, vol. 115, pp. 18–39. DOI: 10.1016/j.jmapro.2024.01.08.

11. Akkurt A. The effect of cutting process on surface microstructure and hardness of pure and Al 6061 aluminium alloy. *Engineering Science and Technology, an International Journal*, 2015, vol. 18 (3), pp. 303–308. DOI: 10.1016/j.jestch.2014.07.004.

12. Gariboldi E., Previtali B. High tolerance plasma arc cutting of commercially pure titanium. *Journal of Materials Processing Technology*, 2005, vol. 160, pp. 77–89. DOI: 10.1016/j.jmatprotec.2004.04.366.

13. Grinenko A.V., Knyazhev E.O., Chumaevskii A.V., Nikolaeva A.V., Panfilov A.O., Cheremnov A.M., Zhukov L.L., Gusarova A.V., Sokolov P.S., Gurianov D.A., Rubtsov V.E., Kolubaev E.A. Structural features and morphology of surface layers of AA2024 and AA5056 aluminum alloys during plasma cutting. *Russian Physics Journal*, 2023, vol. 66, pp. 925–933. DOI: 10.1007/s11182-023-03025-9.

14. Rubtsov V.E., Panfilov A.O., Knyazhev E.O., Nikolaeva A.V., Cheremnov A.M., Gusarova A.V., Beloborodov V.A., Chumaevskii A.V., Ivanov A.N. Development of plasma cutting technique for C1220 copper, AA2024 aluminum alloy, and Ti-1,5Al-1,0Mn titanium alloy using a plasma torch with reverse polarity. *Obrabotka metallov (tekhnologiya, oborudovanie, instrumenty) = Metal Working and Material Science*, 2022, vol. 24, no. 4, pp. 33–52. DOI: 10.17212/1994-6309-2022-24.4-33-52.

15. Sidorov E.A., Grinenko A.V., Chumaevsky A.V., Panfilov A.O., Knyazhev E.O., Nikolaeva A.V., Cheremnov A.M., Rubtsov V.E., Utyaganova V.R., Osipovich K.S., Kolubaev E.A. Patterns of reverse-polarity plasma torches wear during cutting of thick rolled sheets. *Obrabotka metallov (tekhnologiya, oborudovanie, instrumenty) = Metal Working and Material Science*, 2024, vol. 26, no. 3, pp. 149–162. DOI: 10.17212/1994-6309-2024-26.3-149-162.

16. Chumaevskii A.V., Nikolaeva A.V., Grinenko A.V., Panfilov A.O., Knyazhev E.O., Cheremnov A.M., Utyaganova V.R., Beloborodov V.A., Sokolov P.S., Gurianov D.A., Kolubaev E.A. Structure formation in surface layers of aluminum and titanium alloys during plasma cutting. *Physical Mesomechanics*, 2023, vol. 26, pp. 711–721. DOI: 10.1134/S1029959923060103.

17. Boulos M.I., Fauchais P., Pfender E. Plasma torches for cutting, welding and PTA coating. *Handbook of thermal plasmas*. Cham, Springer, 2023. DOI: 10.1007/978-3-319-12183-3_47-2.

18. Grinenko A.V., Chumaevskii A.V., Knjazhev E.O., Gurianov D.A., Sidorov E.A., Kolubaev E.A. Influence of reverse-polarity plasma cutting parameters on structure and surface roughness of aluminum alloys. *Russian Physics Journal*, 2024, vol. 67 (9), pp. 1287–1293. DOI: 10.1007/s11182-024-03246-6.

19. Rubtsov V.E., Panfilov A.O., Knyazhev E.O., Nikolaeva A.V., Cheremnov A.M., Gusarova A.V., Beloborodov V.A., Chumaevskii A.V., Grinenko A.V., Kolubaev E.A. Influence of high-energy impact during plasma cutting on structure and properties of surface layers of aluminum and titanium alloys. *Obrabotka metallov (tekhnologiya, oborudovanie, instrumenty) = Metal Working and Material Science*, 2023, vol. 25, no. 4, pp. 216–231. DOI: 10.17212/1994-6309-2023-25.4-216-231.

20. Shchitsyn V.Yu., Yazovskikh V.M. Effect of polarity on the heat input into the nozzle of a plasma torch. *Welding International*, 2002, vol. 16 (6), pp. 485–487. DOI: 10.1080/09507110209549563.

21. Matushkina I., Anakhov S., Pyckin Yu. Design of a new gas-dynamic stabilization system for a metal-cutting plasma torch. *Journal of Physics: Conference Series*, 2021, vol. 2094, p. 042075. DOI: 10.1088/1742-6596/2094/4/042075.

22. Kudrna L., Fries J., Merta M. Influences on plasma cutting quality on CNC machine. *Multidisciplinary Aspects of Production Engineering*, 2019, vol. 2 (1), pp. 108–117. DOI: 10.2478/mape-2019-0011.

23. Gostimirović M., Rodic D., Sekulić M., Aleksic A. An experimental analysis of cutting quality in plasma arc machining. *Advanced Technologies & Materials*, 2020, vol. 45 (1), pp. 1–8. DOI: 10.24867/ATM-2020-1-001.

Conflicts of Interest

The authors declare no conflict of interest.